Nanoscale Solute Partitioning in Bulk Metallic Glasses

By *Ling Yang, Michael K. Miller, Xun-Li Wang,* Chain T. Liu, Alexandru D. Stoica, Dong Ma, Jonathan Almer,* and *Donglu Shi*

Fundamental understanding of composition variations and morphology in the nanoscale is essential to the design of advanced materials. Partial crystallization or devitrification of bulk metallic glasses (BMGs) results in novel microstructures, with high density (10^{23}–10^{24} m^{-3}) nanocrystalline precipitates evenly distributed in a glassy matrix. These crystalline precipitates are known to impede the propagation of shear bands, and are promising candidates for improving the mechanical properties of BMG alloys.[1–4] However, it has been an experimental challenge to determine the fine structure of these precipitates, and no one technique can provide all the answers. In this paper, we report the experimental study of a multicomponent BMG alloy, $Zr_{52.5}Cu_{17.9}Ni_{14.6}Al_{10}Ti_5$, utilizing several state-of-the-art characterization techniques. Nanoscale solute partitioning due to strong chemical order is revealed at unprecedented detail by a new wide-field atom probe. This level of details is crucial for understanding the interference peaks observed in small-angle X-ray and neutron scattering experiments, an unsolved mystery for over a decade. A core/shell structure is formed as a result of nanoscale solute partitioning, which poisons the growth and helps stabilize the nanocrystalline particles.

$Zr_{52.5}Cu_{17.9}Ni_{14.6}Al_{10}Ti_5$ is a widely studied BMG with excellent glass forming ability.[5–11] Upon devitrification, crystalline precipitates of 10–20 nm diameter emerge, as evidenced by high-resolution transmission electron microscopy.[9] Moreover, Z-contrast imaging, a technique more sensitive to composition distribution, showed high densities of distinct crystalline particles of similar sizes but with fuzzy boundaries.[9] Nanoscale composition fluctuations have been detected by atom probe tomography (APT), and were attributed to nanocrystalline particles.[11] The structure of devitrified $Zr_{52.5}Cu_{17.9}Ni_{14.6}Al_{10}Ti_5$ has also been investigated by small-angle X-ray scattering (SAXS) and small-angle neutron scattering (SANS). While microscopy reveals structural details in a restricted field of view or analysis volume, small-angle scattering yields the average structure over the scattering volume. SANS and SAXS profiles of $Zr_{52.5}Cu_{17.9}Ni_{14.6}Al_{10}Ti_5$ are both characterized by an interference peak.[8–11] However, there has been no satisfactory analysis of the experimental data that could identify the underlying structure. Although composition fluctuations due to spinodal decomposition can produce interference peaks,[12,13] no composition wave with a characteristic wavelength was detected experimentally. Instead, well-defined crystalline particles were reported by microscopy experiments.[9,11] Mathematically, the interference peak could also be generated by second-phase particles with a depleted diffusion zone.[14,15] However, experimental determination of the fine-scale composition variations in zirconium-based alloys is difficult with traditional voltage-pulsed APT, due to their poor electrical conductivities and brittleness at cryogenic temperatures. As a result, the structure of nanocrystalline particles in BMG alloys has remained a mystery.

We have recently conducted an experimental study using a new atom-probe equipped with a high-repetition pulsed laser,[16] together with in situ SAXS. With these two complementary techniques, and making use of previously reported SANS data,[8] the structure of nanocrystalline particles of devitrified $Zr_{52.5}Cu_{17.9}Ni_{14.6}Al_{10}Ti_5$ is established.

Two specimens were characterized by APT; one in the as-cast condition, and the other after isothermal annealing for 900 min at 663 K. For the as-cast sample, the APT analysis revealed a homogeneous microstructure characteristic of a completely amorphous state. On the other hand, the sample annealed for 900 min at 663 K showed a two-phase microstructure, consisting of lens-shaped precipitates and the surrounding matrix. Portions of several[9] impinging precipitates, contained in a 70 nm × 70 nm × 200 nm box, were extracted from the atom-probe data, and are shown in Figure 1a. Many of the precipitates are partially obscured by others, and the full extent of the precipitates is cropped by the bounding box. The red isoconcentration surface is constructed at 52% Zr, a concentration that is representative of the precipitate/matrix interface. This isoconcentration surface reveals the lenticular shape of each precipitate. The size, position, and orientation of the atom-probe data were selected to reveal the full extent of the upper precipitate. The upper portion of the red Zr isoconcentration surface of this precipitate has been removed, in order to reveal the Al-enriched core in the interior of the precipitate. The core region is denoted by the yellow isoconcentration surface, constructed of 5.4% Al. A rough estimate indicates a precipitate number density on the order of 10^{23} m^{-3}.

[*] Dr. L. Yang, Dr. X. Wang, Dr. A. D. Stoica, Dr. D. Ma
Neutron Scattering Science Division
Oak Ridge National Laboratory
Oak Ridge, TN 37831 (USA)
E-mail: wangxl@ornl.gov
Dr. L. Yang, Prof. D. Shi
Department of Chemical and Materials Engineering
University of Cincinnati
Cincinnati, OH 45221-0012 (USA)
Dr. M. Miller, Dr. C. Liu
Materials Science and Technology Division
Oak Ridge National Laboratory
Oak Ridge, TN 37831 (USA)
Dr. C. Liu
Department of Materials Science and Engineering
University of Tennessee
Knoxville, TN 37919 (USA)
Dr. J. Almer
Advanced Photon Source, Argonne National Laboratory
Argonne, IL 60439 (USA)

DOI: 10.1002/adma.200801183

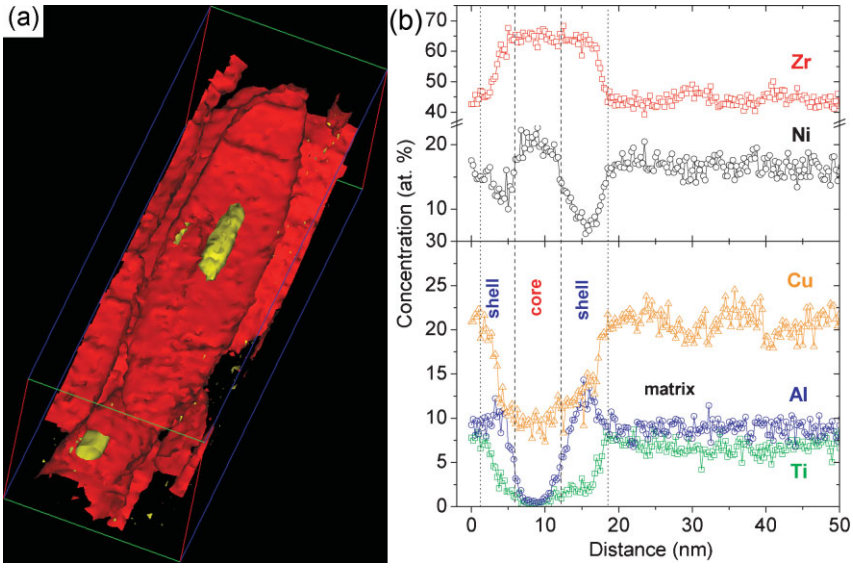

Figure 1. a) Isoconcentration surfaces determined by APT, revealing the lenticular shape of Zr-enriched precipitates and the internal Al-enriched core regions. The red (52% Zr) and yellow (5.4% Al) isoconcentration surfaces delineate the precipitate/matrix and the precipitate/core interfaces, respectively. The encompassing box is 70 nm × 70 nm × 200 nm in extent. b) Linear composition profiles through the center of a lenticular precipitate. Al atoms are rejected from the core, while Ti atoms are rejected from both the core and the shell.

Figure 1b shows a linear composition profile through the center of one of the lenticular precipitates, revealing details of the solute partitioning between core, shell, and surrounding matrix. Well-defined particles are observed, as indicated particularly by the constant concentration profile of Zr atoms. Ti atoms are rejected from the core and shell to the matrix. Al atoms are also rejected from the core, while there is an increased Al concentration in the shell. In fact, the core and shell show opposite trends for solute partitioning for Ni and Al. The average compositions of the core, shell, and matrix are summarized in Table 1. The core has an approximate composition Zr_2M (see the last column of Table 1), where M = (Ni, Cu), consistent with the crystalline phase identified by X-ray diffraction.[6,10] The composition of the shell is also close to Zr_2M, with various amounts of Al, Ni, and Cu in place of M. The structure of the shell is most likely of Zr_2Ni type as well, since no other crystalline phases were identified in the X-ray diffraction pattern at this annealing temperature. Indeed, metastable Zr_2Al can exist as several polymorphs,[17] one of which is isostructural with tetragonal Zr_2Ni.[18]

To understand why such partitioning takes place, it was instructive to compare the heat of mixing of select constituent elements,[19] which are listed in Table 2. Zr–Ni has the largest negative heat of mixing ($-49\,kJ\,mol^{-1}$), and therefore the strongest chemical bonding. Clearly, the strong Zr–Ni bond is the driver of solute partitioning, which explains the composition of the core. Al also bonds strongly with Zr ($-44\,kJ\,mol^{-1}$), explaining the enhanced Al concentration in the shell. Cu atoms show an intermediate level of heat of mixing with both Zr ($-23\,kJ\,mol^{-1}$) and Al ($-1\,kJ\,mol^{-1}$), and are fillers in both the core and shell. Indeed, both (Ni, Cu)- and (Al, Ti)-centered Zr clusters have been identified in the as-cast sample.[20] Ti atoms do not bond well with Zr ($0\,kJ\,mol^{-1}$), justifying their expulsion to the matrix upon annealing.

We now turn to the analysis of the small angle scattering data, which provides a perspective of the average structure. A representative SAXS pattern measured after annealing at 670 K for 120 min and the corresponding SANS pattern that was measured by Loffler et al.[8] on a sample of similar nominal composition after annealing at 686 K for 576 min, are shown in Figure 2. Both are characterized by an interference peak centered on $Q \sim 0.02$–0.03 Å^{-1}.

We find that the SAXS and SANS data are both well described by a core/shell structure model with a log-normal particle-size distribution. The basic idea of a core/shell structure was described by Guinier and Fourner in their explanation of the interference peak in the SAXS data of age-hardening Al–Ag alloys.[21] The scattering intensity from monodisperse spherical particles with a core/shell structure is given by[22]

$$I(Q) = \frac{k}{V_S}\left[3V_C(\rho_C - \rho_S)\Phi(QR_C) + 3V_S(\rho_S - \rho_M)\Phi(QR_S)\right]^2 \quad (1)$$

where $\Phi(x) = (\sin x - x\cos x)/x^3$, R is the radius, V is the volume, and ρ is the scattering length density. The subscripts C, S, and M denote the core, shell, and matrix, respectively. k is a scale factor and $\Phi(x)$ is a function that peaks at $Q = 0$ and falls monotonously at small Q values. If $(\rho_C - \rho_S)$ and $(\rho_S - \rho_M)$ have opposite signs, the competition between the two terms will lead to an interference peak in the small Q region. A log-normal distribution function is assumed for the volume fraction of R_S, with two parameters: $R_0$the center, and ln $\sigma$the width. This particle-size distribution also accounts for the lenticular shape of the crystalline particles. To describe the sharp intensity rise at low Q values in the SAXS data, a term is introduced, corresponding to

Table 1. Representative compositions (in %) of the phases as determined by APT. The estimated standard deviations 2σ are based on the counting statistics of the measurements, $\sigma = \sqrt{c(1-c)/n}$, where n is the number of atoms in the measurements.

	Zr	Cu	Ni	Al	Ti	Cu + Ni + Al
Core	67.1 ± 1.2	9.8 ± 0.7	22.0 ± 1.0	0.6 ± 0.2	0.4 ± 0.1	32.4 ± 1.2
Shell	65.0 ± 0.2	12.0 ± 0.2	8.5 ± 0.1	12.4 ± 0.2	2.1 ± 0.1	32.9 ± 0.3
Matrix	44.8 ± 0.1	21.5 ± 0.1	12.6 ± 0.1	8.9 ± 0.1	7.2 ± 0.1	43.0 ± 0.2
Nominal	52.5	17.9	14.6	10.0	5.0	42.5

Table 2. Heat of mixing (kJ mol^{-1}) for select elements in the alloy.[19]

Zr–Ni	Zr–Al	Zr–Cu	Zr–Ti	Al–Cu	Al–Ni
−49	−44	−23	0	−1	−22

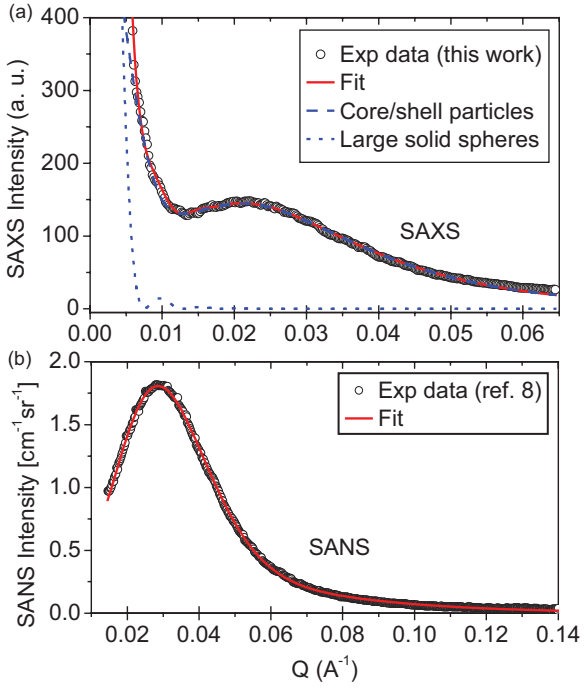

Figure 2. Representative small-angle scattering patterns of $Zr_{52.5}Cu_{17.9}Ni_{14.6}Al_{10}Ti_5$ and a core/shell model fit. The SAXS data were obtained during isothermal annealing at 670 K for 120 min. The contributions from core/shell particles and monodisperse large spheres are plotted as dashed lines. SANS data were obtained during isothermal annealing at 686 K for 576 min.[8] Note that the Q ranges for SAXS and SANS are slightly different.

scattering by monodisperse solid sphere particles with larger sizes, R_b. The combined scattering yields

$$I(Q) = k\left\{\int_0^\infty R_S^3 . w(R_S, [R_0, \sigma])[\eta t^3 \Phi(QR_S t) - \Phi(QR_S)]^2 dR_S + k_b \Phi(QR_b)^2\right\} \quad (2)$$

where $w[R_S, (R_0, \sigma)]$ is the log-normal distribution function for R_S and k_b is a separate scale factor. Two ratios are introduced here: $t = R_C/R_S$ and $\eta = (\rho_C - \rho_S)/(\rho_M - \rho_S)$.

Satisfactory fits to the SAXS and SANS data were obtained, as shown in Figure 2. In particular, the interference peaks in both sets of data were well captured. The scattering intensities from core/shell particles and the large solid spheres are also plotted as dotted lines. Clearly, the latter contributes only to the low-Q part of the SAXS intensity.

The fitted core/shell ratios, t, are similar for SAXS and SANS, (0.78 ± 0.04) and (0.75 ± 0.02) respectively. The corresponding scattering contrast ratios η are (1.6 ± 0.3) and (2.6 ± 0.1). We also attempted to evaluate η based on the composition data in Table 1. The calculated η (with no adjustable parameters) is 1.71 for the SAXS data, in excellent agreement with the parameter determined by the core/shell model. Since no detailed composition profile is available for the SANS sample, precise evaluation of η could not be carried out. Nonetheless, using the compositions in Table 1, a η value of 1.75 was estimated for the SANS data. Although this value is smaller than the fitted parameter of 2.6, it has the correct sign. It is remarkable that a delicate balance in chemical composition produced a positive η, and hence the interference peak for both SAXS and SANS. A closer look into η calculations shows that the increased Ni composition in the core is the main cause for $\rho_C > \rho_S$, whereas the depletion of (Ni, Cu) atoms in the shell layer causes $\rho_S < \rho_M$.

From the fit to the SAXS data the diameter of the nanocrystalline precipitates ($2R_0$, including the shell) was found to be (22.6 ± 0.2) nm, and the shell thickness (2.5 ± 0.1) nm. For SANS, corresponding values of (18.8 ± 0.4) and (2.4 ± 0.1) nm were obtained. The nature of the large particles ($R_b = (59.2 \pm 0.5)$ nm) was not identified in the SAXS data. One possibility, in agreement with Figure 1a, is that they are aggregates of core/shell particles.

Having established the model, we fitted the SAXS data throughout the annealing process (at 673 K, for 240 min.). Figure 3 shows R_0 and η as a function of annealing time. R_0 grows rapidly initially, approaching an equilibrium value asymptotically. In fact, the evolution of R_0 is fairly well described by $R_0(t) = R_0^{max}\{1 - \exp[-(t/\tau)^d]\}$, equation similar to the growth function in John–Mehl–Avrami (JMA) theory, which estimates the volume fraction of transformed materials.[8,10] The fitted parameters are $R_0^{max} = (12.4 \pm 0.2)$ nm, $d = (0.23 \pm 0.02)$, and $\tau = (2.1 \pm 0.2)$ s. The fitted η shows larger scatter, but the general trend is characterized by a long decline with increasing annealing time. Note that in the absence of a shell, $\eta = 0$ ($\rho_C = \rho_S$). Given the slow growth of the core/shell particles, this result strongly suggests that the whole particle was transformed during initial crystallization, followed by re-partitioning of constituent elements between the core and the shell.

In summary, by leveraging the power of several state-of-the-art experimental tools, we have resolved the structure of nanocrystalline particles in devitrified $Zr_{52.5}Cu_{17.9}Ni_{14.6}Al_{10}Ti_5$. A core/shell structure develops due to nanoscale solute partitioning, and is responsible for the interference peaks observed in SAXS and SANS experiments. Interference peaks have also been observed

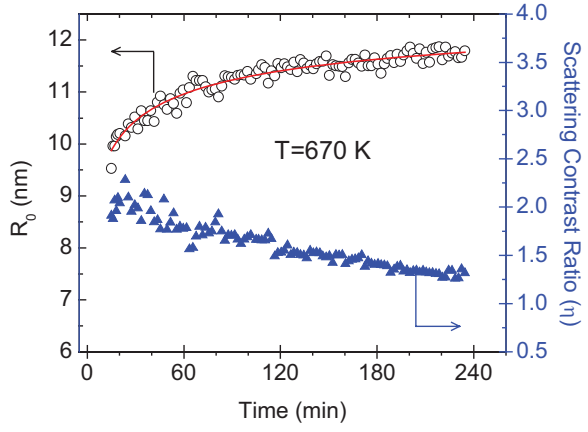

Figure 3. Evolution of the particle radius (R_0) and scattering contrast ratio (η) as a function of annealing time. The solid line is the fit to a growth function (see text). The annealing temperature was 670 K. The first two data points for η were ignored because of the large error bars resulting from weak interference peaks.

in other BMG alloys, notably $Zr_{41.2}Ti_{13.8}Cu_{12.5}Ni_{10}Be_{22.5}$,[23] $Mg_{62}Cu_{25}Y_{10}Li_3$,[24] and ternary $Mg_{65}Cu_{25}Tb_{10}$ and $Zr_{60}Cu_{30}Tb_{10}$,[25] suggesting that the core/shell structure is a common feature of nanocrystallization in BMG alloys. The question of whether the nanoscale core/shell structure could be manipulated in materials design to improve their properties is still unanswered.

Our results have important implications in understanding the mechanisms of nucleation and growth of nanocrystalline precipitates and the stability of BMG alloys. Apparently, upon annealing crystalline precipitates nucleate by a combination of chemical segregation and atomic ordering, which leads to a core/shell structure. This nucleation process is interface-controlled, and involves only neighboring atoms.[10,26] In the case of $Zr_{52.5}Cu_{17.9}Ni_{14.6}Al_{10}Ti_5$, the core has an approximate composition Zr_2(Ni, Cu), and is indeed Ni-rich, as suggested by previous in situ experiments using synchrotron X-ray.[10] Further growth of the crystalline precipitates is governed by long-range volumetric diffusion, as the Ni concentration in the surrounding area is depleted. Nucleation of the Zr_2(Ni, Cu) core also results in Al expulsion into the region surrounding the core, forming a shell. The strong bonding between Al and Zr and the limited diffusion of Al in the glass maintains the increased Al composition in the Ni-poor shell region. This further poisons the growth of the crystalline precipitates. The combination of chemistry-driven nucleation dynamics and poisoned growth helps to stabilize the composite structure, with high-density nanocrystalline precipitates uniformly distributed in a glassy matrix.

Experimental

The BMG samples were prepared by a drop-casting method, and were characterized by a variety of techniques [5–7,10]. The glass and crystallization temperatures were 628 and 714 K, respectively, as determined by differential scanning calorimetry at a heating rate of 10 K min^{-1}. APT was performed using a wide field of view, laser-pulsed local-electrode atom probe (LEAP), with a specimen temperature of 60 K [16]. Atoms were field-evaporated with a focused 12 ps laser pulse (wavelength 532 nm) operated at a pulse repetition rate of 250 kHz. Two specimens were characterized, one in the as-quenched condition and the other after isothermal annealing for 900 min at 663 K. With this new atom probe, datasets containing almost a quarter of a billion atoms have been collected. This represents an almost four orders of magnitude improvement in the analyzed volume, compared to previous data[11].

SAXS experiments were performed using the high-energy synchrotron beam ($E = 80$ keV) at sector 1-ID at Advanced Photon Source (APS), Argonne National Laboratory. The experimental set up has been reported elsewhere [10,27]. The beam size was 0.1 mm × 0.1 mm, and the samples were 1 mm thick disks with a diameter of 8 mm. The use of a high-energy synchrotron beam ensures that the measurements are representative of the bulk. The BMG samples were heated with a rate of 10 K min^{-1} to 670 K, and isothermally annealed at this temperature for more than 240 min. The small-angle scattering data were recorded in situ every 30 s.

Acknowledgements

This research was supported by the Office of Basic Energy Sciences, US Department of Energy, under Contract DE-AC05-00OR22725 with UT-Battelle, LLC. Use of APS was supported by the US Department of Energy under contract no. DE-AC02-06CH11357. Research at the Oak Ridge National Laboratory SHaRE User facility was sponsored by the scientific user facilities Division, Office of Basic Energy Sciences, U.S. Department of Energy. Helpful discussions with Dr. J. R. Morris are gratefully acknowledged.

Received: April 29, 2008
Revised: August 1, 2008
Published online:

[1] M. Chen, A. Inoue, W. Zhang, T. Sakurai, *Phys. Rev. Lett.* **2006**, *96*, 245502.
[2] C. Fan, D. V. Louzguine, C. F. Li, A. Inoue, *Appl. Phys. Lett.* **1999**, *75*, 340.
[3] C. Fan, C. F. Li, A. Inoue, V. Haas, *Phys. Rev. B* **2000**, *61*, R3761.
[4] C. Fan, A. Inoue, *Appl. Phys. Lett.* **2000**, *77*, 46.
[5] J. G. Wang, B. W. Choi, T. G. Nieh, C. T. Liu, *J. Mater. Res.* **2000**, *15*, 798.
[6] T. G. Nieh, J. Wadsworth, C. T. Liu, G. E. Ice, K. S. Chung, *Mater. Trans.* **2001**, *42*, 613.
[7] C. T. Liu, M. F. Chisholm, M. K. Miller, *Intermetallics* **2002**, *10*, 1105.
[8] J. F. Loffler, S. Bossuyt, S. C. Glade, W. L. Johnson, W. Wagner, P. Thiyagarajan, *Appl. Phys. Lett.* **2000**, *77*, 525.
[9] E. Pekarskaya, J. F. Loffler, W. L. Johnson, *Acta Mater.* **2003**, *51*, 4045.
[10] X. L. Wang, J. Almer, C. T. Liu, Y. D. Wang, J. K. Zhao, A. D. Stoica, D. R. Haeffner, W. H. Wang, *Phys. Rev. Lett.* **2003**, *91*, 265501.
[11] A. A. Kundig, M. Ohnuma, T. Ohkubo, K. Hono, *Acta Mater.* **2005**, *53*, 2091.
[12] J. W. Cahn, *J. Chem. Phys.* **1965**, *42*, 93.
[13] J. Mainville, Y. S. Yang, K. R. Elder, M. Sutton, K. F. Ludwig, G. B. Stephenson, *Phys. Rev. Lett.* **1997**, *78*, 2787.
[14] H. Hermann, A. Wiedenmann, P. Uebele, *Phys. B* **1997**, *241*, 352.
[15] H. Hermann, A. Heinemann, H. D. Bauer, N. Mattern, U. Kuhn, A. Wiedenmann, *J. Appl. Cryst.* **2001**, *34*, 666.
[16] T. F. Kelly, M. K. Miller, *Rev. Sci. Instrum.* **2007**, *78*, 031101.
[17] E. Clouet, J. M. Sanchez, C. Sigli, *Phys. Rev. B* **2002**, *65*, 094105.
[18] Powder Diffraction File No. 14-0436, International Centre for Diffraction Data, Newton Square, PA, USA **1981**.
[19] F. R. D. Boer, in *Cohesion in Metals: Transition Metal Alloys, North-Holland*, Elsevier Scientific Publishing Co., New York, USA **1988**.
[20] D. Ma, A. D. Stoica, L. Yang, X. L. Wang, Z. P. Lu, J. Neuefeind, M. J. Kramer, J. W. Richardson, T. Proffen, *Appl. Phys. Lett.* **2007**, *90*, 211908.
[21] A. Guinier, G. Fournet, in *Small-angle Scattering of X-rays*, Wiley, New York, U.S.A. **1978**.
[22] J. S. Pedersen, *Adv. Colloid Interface Sci.* **1997**, *70*, 171.
[23] S. Schneider, P. Thiyagarajan, W. L. Johnson, *Appl. Phys. Lett.* **1996**, *68*, 493.
[24] W. Liu, W. L. Johnson, S. Schneider, U. Geyer, P. Thiyagarajan, *Phys Rev B* **1999**, *59*, 11755.
[25] L. Yang, X. L. Wang, unpublished.
[26] L. Yang, X.-L. Wang, W. D. Porter, Z. P. Lu, A. D. Stoica, E. A. Payzant, J. Almer, D. Shi, *Adv. Eng. Mater.* in press.
[27] APS Science, The Annual Report of the Advanced Photon Source at Argonne National Laboratory, ANL-04/07, Argonne National Laboratory, Argonne, USA.